

# Deformable Image Registration using Neural ODEs

Yifan Wu\* Tom Z.Jiahao\* Jiancong Wang\* Paul A. Yushkevich James C. Gee M. Ani Hsieh

University of Pennsylvania, Philadelphia, PA, USA

{yfwu, zjh}@seas.upenn.edu {jiancong.wang, pauly2}@pennmedicine.upenn.edu

gee@upenn.edu mya@seas.upenn.edu

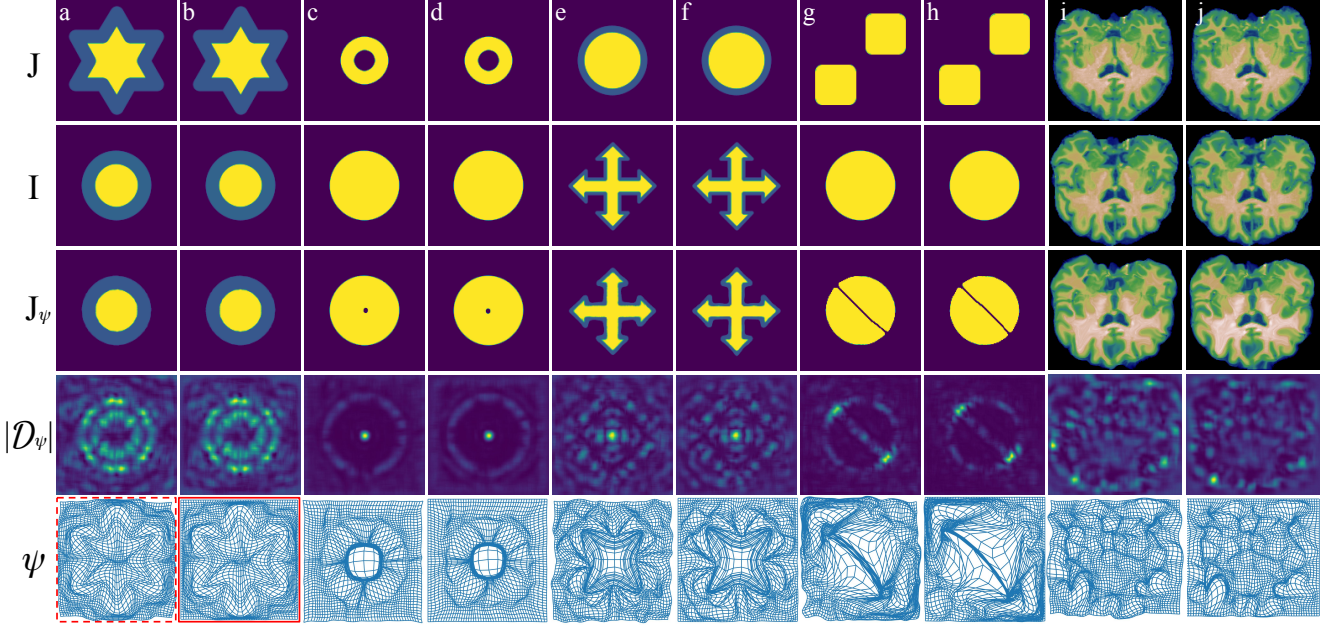


Figure 1: **2D image registration using our framework.** The rows show ( $J$ ) the moving images, ( $I$ ) fixed images, ( $J_\psi$ ) warped moving images, ( $|D_\psi|$ ) Jacobian determinants of the transformation  $\psi$ , and ( $\psi$ ) grid visualization of  $\psi$  respectively. The columns (b)(d)(f)(h)(j) incorporate a fixed boundary constraints while (a)(c)(e)(g)(i) do not.

## Abstract

Deformable image registration, aiming to find spatial correspondence between a given image pair, is one of the most critical problems in the domain of medical image analysis. In this paper, we present a generic, fast, and accurate diffeomorphic image registration framework that leverages neural ordinary differential equations (NODEs). We model each voxel as a moving particle and consider the set of all voxels in a 3D image as a high-dimensional dynamical system whose trajectory determines the targeted deformation field. Compared with traditional optimization based methods, our framework reduces the running time from tens of minutes to tens of seconds. Compared with recent data-driven deep learning methods, our framework is more accessible since it does not require large amounts of training data. Our experiments show that the registration results of

our method outperform the-state-of-arts under various metrics, indicating that our modeling approach is well fitted for the task of deformable image registration.

## 1. Introduction

Deformable image registration (DIR) is a well-studied problem in modern medical image analysis, because of its broad range of applications including normalization of population studies, quantifying changes in longitudinal imaging, accounting for motions of organ, and as a building block of other image analysis algorithms. DIR is a process for establishing spatial correspondence between image pairs, and the term “deformable” points to the nonlinear and dense nature of the required transformation [21].

The wide range of applications of DIR have sparked developments in several directions. One body of work searches for a mapping/deformation field by optimizing a

\*Equal contribution.

similarity objective between a pair of images, requiring the mapping between the images and its inverse to be smooth. This requirement is motivated by the fact that in medical applications, the common practice of warping canonical templates to describe anatomy predicates on the preservation of topology [14]. This requirement is also known as *diffeomorphism* if both images reside on smooth manifolds. Intuitively, diffeomorphism requires the deformation field to not create or remove holes, folds or self-intersections on smooth manifolds. Two prominent developments in optimization based methods are Large Deformation Diffeomorphic Metric Mapping (LDDMM) [7, 18] and Advanced Normalization Tools (ANTs), also referred to as SyN [5]. While LDDMM achieves diffeomorphism by modeling the image grid as a flow field and composing small steps of deformation described by a system of differential equations, ANTs heuristically search for an invertible and smooth deformation field (and therefore diffeomorphic) via a process called fixed point iteration [5].

With rapid advancement in machine learning and abundance of medical imaging data, there is increased interest in developing deep learning based methods to solve the DIR problem. Notably, many techniques focus on addressing the slowness of traditional optimization based methods [25, 6, 11, 19, 12, 12, 3, 20]. These methods train deep neural networks to represent deformation fields for a large training set of image pairs, thereby capturing a common representation for a collection of images. After training, registration on a new image pair therefore becomes a rapid inference process. However, one current limitation stems from the assumption that the new pair of images to be registered comes from the same distribution as the training data which is often not valid in real-world settings. In particular, in industrial/hospital use cases, the myriad of factors such as the type of imaging machines, image resolutions, and data pre-processing practices may all contribute to a potential distribution shift in the incoming images. Furthermore, the large number of different organs (*e.g.*, brain, lung) and imaging modalities (*e.g.*, MRI, CT) can make it impractical to train a model for every possible combination. Moreover, there are often cases where training data is not available such as human brain histology images for Alzheimer’s studies [2] or mouse brain images for the brain connectome project [24] since such data are extremely rare and difficult to collect. As such, recent data driven learning based methods are hard to generalize, precluding their widespread adoption.

In this work, we propose an optimization based method for performing registration on 3D MRI scan images. We combine the best from both worlds by leveraging the expressiveness of deep neural networks and modern optimization algorithms to swiftly discover diffeomorphic maps between medical image pairs. Our method borrows intuition from dynamical systems and explicitly models the de-

mation field as a high-dimensional non-autonomous ordinary differential equation. Specifically, we treat the set of all voxel locations (or pixel locations in the case of 2D images) in an image as one single evolving system, and parametrize its dynamics with a deep neural network. The registration task therefore becomes finding one of its trajectories whose end point is the deformation field which minimizes the dissimilarity between image pairs. The benefits of our approach are twofold. First, by explicitly modeling the image grid as one high-dimensional system, we can leverage convolutional layers to allow voxels to spatially interact with each other within the system dynamics. Second, our framework makes embedding dynamical constraints such as spatial smoothing straightforward. As such, the proposed framework is flexible with respect to model choice and can easily incorporate boundary conditions on demand. Additionally, we leverage the adjoint sensitivity method [8], which enables constant-memory gradient propagation with respect to the number of steps taken by the system, significantly reducing the memory cost for registration tasks requiring smooth interpolation along the deformation path. In contrast, LDDMM is akin to spatially-discretizing a flow field and modeling its dynamics with a system of low-dimensional differential equations. LDDMM generally impose more constraints due to the discretization.

Overall, the contributions of this paper are: (1) generalization of the flow field approach to registration through high-dimensional dynamical system modeling, (2) development of a fast and memory-efficient optimization based registration method on medical images, and (3) demonstrations that the proposed framework outperforms state-of-the-art (SOTA) registration methods using a variety of metrics.

## 2. Problem Formulation

The deformable image registration problem can be formulated as follows: consider an unparametrized 3D image as a discrete solid, where the location of the  $i^{th}$  voxel/point is given by  $\mathbf{x}_i \in \Omega \subseteq \mathbb{R}^3, i \neq j \iff \mathbf{x}_i \neq \mathbf{x}_j$ . This voxel location is known in shape analysis as a landmark coordinate. The location of all voxels or the voxel cloud can be denoted by the ordered set  $q \in \mathbb{R}^{D \times H \times W} \times \Omega$ , where  $D, H$ , and  $W$  are the image depth, height and width respectively. As a shorthand, we write  $\Pi = \mathbb{R}^{D \times H \times W} \times \Omega$  as the domain of voxel clouds. We denote the fixed image by  $I$  and the moving image by  $J$ , which are functions  $I, J : \Omega \rightarrow \mathbb{R}^d$ , mapping each voxel coordinate to the voxel value/intensity. In this work, we only consider scalar-valued MRI images, and therefore  $d = 1$ .

Traditionally, the goal of DIR is to find some *good* transformation  $\phi : \Omega \rightarrow \Omega$  such that the transformed moving image  $J(\phi(\mathbf{x}))$ ,  $\forall \mathbf{x} \in q$  is similar to the fixed image  $I$  [7]. Here,  $\phi$  is the spatial transformation that maps the domain of voxels  $\Omega$  onto itself. An identity map is de-

defined as  $\phi_0$  such that  $\phi_0(\mathbf{x}) = \mathbf{x}$ . In many applications of DIR, a *good* transformation  $\phi$  is both sufficiently smooth and diffeomorphic in  $\mathbb{R}^3$  [4, 7]. The latter condition requires that the topology of the moving image is preserved under transformation. In other words, the transformation  $\phi$  should not create holes or folds in  $\Omega$ . We can overload the function  $\phi$  by defining its application on a voxel cloud as a point-wise transformation on the voxels, i.e.  $\phi(q_f) = (\phi(x_1), \phi(x_2), \dots, \phi(x_N))^T$ , where  $q_f = (x_1, x_2, \dots, x_N)^T$  is the spatially flattened voxel cloud ( $N = D \times H \times W$  is the total number of points in the voxel cloud). Similarly, this point-wise transformation can be defined for image  $J$  when applied on a transformed voxel cloud.

Following the above definitions, DIR is generally formulated as the minimization of the combined image similarity metric and regularization of the transformation given by

$$\mathcal{J}(\phi; I, J) = \mathcal{S}(J(\phi(q_0)), I) + \mathcal{R}(\phi), \quad (1)$$

where  $q_0$  is the initial voxel cloud when none of the voxels in the cloud has undergone transformation. The term  $\mathcal{S}(\cdot, \cdot)$  is the similarity metric that measures the difference between the deformed moving image  $J$  and the fixed image  $I$ . The term  $\mathcal{R}(\cdot)$  is the regularizer which often takes the form of an energy function.

However, in this work, we reformulate the problem by searching for a transformation  $\psi : \Pi \rightarrow \Pi$  which maps the domain of the voxel cloud  $\Pi$  onto itself, while requiring smoothness and diffeomorphism in  $\Pi$ . This is a marked contrast with LDDMM, where  $\phi$  does not assume interaction among the voxels [7]. In this work, we explicitly allow interactions among voxels by searching for a transformation in the high-dimensional cloud space. Our problem formulation has a similar form as Eqn. (1), with the exception that the transformation over the voxel cloud is no longer point-wise, but instead given by

$$\mathcal{J}(\psi; I, J) = \mathcal{S}(J(\psi(q_0)), I) + \mathcal{R}(\psi), \quad (2)$$

where  $\psi(q_f) = (\psi(x_1, x_2, \dots, x_N))^T$ . We can alternatively write it as  $\psi(q_f) = (\psi_1(q_f), \psi_2(q_f), \dots, \psi_N(q_f))^T$ , where  $\psi_i$  is called the  $i^{th}$  component of the  $\psi$ . Our formulation is motivated by two facts. First, convolutional neural network (CNN) layers have enabled significant decrease in the number of neural network parameters by reducing the dimensionality of images. This makes computing the transformation over an entire voxel cloud computationally feasible. Second, in the traditional formulation, low-dimensional transformations (e.g. affine transformations) perform poorly because of the complexity inherent to the registration task. As a result, since the emergence of DIR, most works have focused on producing high-dimensional non-rigid transformations, which are specified at each voxel location. This makes it natural to directly

search for high-dimensional transformations in the domain of the voxel cloud. We will demonstrate that this problem reformulation will afford both competitive performance and greater model flexibility.

### 3. Method

#### 3.1. Dynamical System View

Our work borrows intuition from dynamical systems and treats the trajectory of the entire voxel cloud as the solution to a first-order non-autonomous ordinary differential equation given by

$$\begin{aligned} \frac{dq}{dt} &= \mathcal{K} \mathbf{v}_\theta(q(t), t), \\ \text{s.t. } q(0) &= q_0, \end{aligned} \quad (3)$$

where  $\mathbf{v}_\theta(\cdot)$ , as parametrized by  $\theta$ , is the vector field describing the dynamics of the voxel cloud,  $\Pi$  is the state space, and  $q_0$  is the initial condition at  $t = 0$ . We employ Gaussian kernels (for  $\Omega \subseteq \mathbb{R}^3$ , we use 3D Gaussian kernels), denoted by  $\mathcal{K}$ , as a filtering operator to enforce spatial smoothness in  $\Omega$ . Intuitively  $\mathcal{K}$  is to ensure that the velocities of voxels are similar to those of their neighbors. Increasing the kernel size amounts to smoothing over larger voxel space, and therefore will improve the smoothness of the resulting flow; increasing the variance of the kernel amounts to encouraging more individual movements and therefore reduces the smoothness of the resulting flow.

The term *non-autonomous*, or equivalently *time-variant/non-stationary* means that the time derivative of  $q$  explicitly depends on  $t$  [22]. In other words, the velocity field attached to the Eulerian frame changes with time, as in the case of LDDMM. However, unlike methods such as LDDMM [4, 7] which compute the trajectory by composing velocity field attached to the Eulerian frame, we instead follow voxels along their trajectories.

The trajectory of  $q$  is generated by integrating the ODE in Eqn. (3) with the initial condition  $q_0$ . Assuming that the voxel cloud evolves from  $t = 0$  to  $t = s$ , the resulting voxel cloud at  $t = s$  denotes the transformation  $\psi(q_0)$  given by

$$\psi(q_0) = q(s) = q_0 + \int_0^s \mathcal{K} \mathbf{v}_\theta(q(t), t) dt. \quad (4)$$

Eqn. (4) is referred to as a diffeomorphic flow map in dynamical systems. While the uniqueness and existence theorem [22] only implies diffeomorphism in the high-dimensional space  $\Pi$ , we will show that diffeomorphism can be achieved in  $\Omega$  by incorporating soft constraints in the optimization task. In practice, the flow map is computed using a numerical integration scheme such as the Euler's method. Note that while  $s$  is chosen to be 1 in most existing works, it can be parametrized by the total number of steps taken by the solver and the corresponding step sizes. The task of finding the transformation  $\psi$  therefore becomes

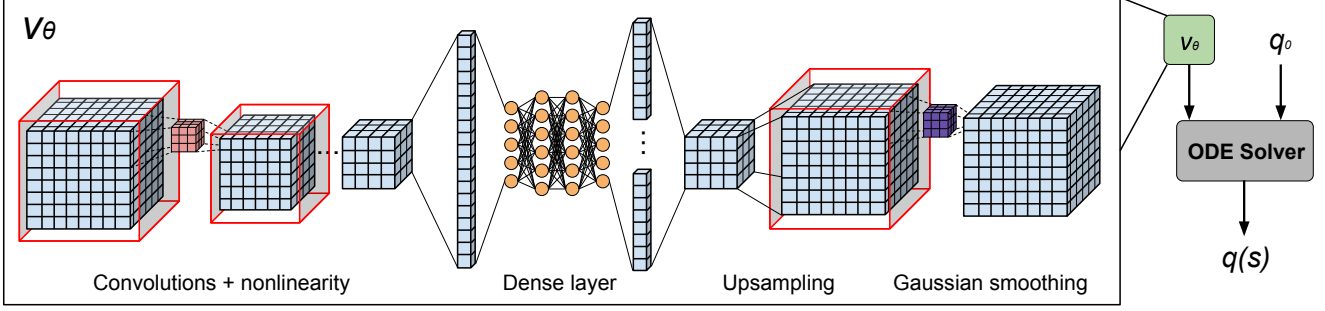


Figure 2: **Framework overview.** Our frame models the vector field  $\mathbf{v}_\theta$  as a neural network. A voxel cloud first gets down-sampled using convolutional layers. It then passes through dense layers where time is injected. It then gets upsampled and restored back to the shape of the voxel cloud and smoothed with a gaussian kernel.

finding the best set of parameters describing  $\mathbf{v}$ . The optimization problem therefore becomes:

$$\theta = \arg \min_{\theta \in \Theta} \mathcal{L}_{sim} \left( I, J(q_0 + \int_0^s \mathcal{K} \mathbf{v}_\theta(q(t), t) dt) \right) + \mathcal{R}(\psi, \mathbf{v}_\theta) + \mathcal{B}(\psi), \quad (5)$$

where  $\Theta$  is the space of all possible parameters. The different components in the loss function include the similarity metric  $\mathcal{L}_{sim}$ , the regularizers  $\mathcal{R}$ , and the boundary conditions  $\mathcal{B}$ . The similarity loss is  $\mathcal{L}_{sim}(I, J) = 1 - NCC(I, J)$ , where  $NCC$  is the normalized cross correlation given by

$$NCC(I, J) = \frac{\frac{1}{N} \sum_{\mathbf{x} \in q(s)} \sum_{\mathbf{x}_i} (I(\mathbf{x}_i) - \bar{I}(\mathbf{x})) (J(\mathbf{x}_i) - \bar{J}(\mathbf{x}))}{\sqrt{\sum_{\mathbf{x}_i} (I(\mathbf{x}_i) - \bar{I}(\mathbf{x}))^2 \sum_{\mathbf{x}_i} (J(\mathbf{x}_i) - \bar{J}(\mathbf{x}))^2}}, \quad (6)$$

where  $\bar{I}(\mathbf{x})$  and  $\bar{J}(\mathbf{x})$  are the local mean of a size  $w^3$  window with  $\mathbf{x}$  being at its center position and  $\mathbf{x}_i$  is an element within this window. In this work we set  $w$  as 21.

The regularization term consists of three terms:

$$\mathcal{R}(\psi, \mathbf{v}_\theta) = \lambda_1 \mathcal{L}_{Jdet} + \lambda_2 \mathcal{L}_{mag} + \lambda_3 \mathcal{L}_{smt}. \quad (7)$$

The first term,  $\mathcal{L}_{Jdet}$ , penalizes negative Jacobian determinants in the transformed voxel cloud and is given by

$$\mathcal{L}_{Jdet} = \frac{1}{N} \sum_{\mathbf{x} \in q(s)} \sigma(-(|\mathcal{D}_\psi(\mathbf{x})| + \epsilon)), \quad (8)$$

where  $\mathcal{D}_\psi(\mathbf{x})$  is the Jacobian matrix at  $\mathbf{x}$  under the transformation  $\psi$ . If there are no holes or folds created by transformation, its determinant  $|\mathcal{D}_\psi(\mathbf{x})|$  should be positive. Here  $\sigma(\cdot) = \max(0, \cdot)$  is the ReLU activation function, which is used to select only negative Jacobian determinants. Lastly, we add a small number  $\epsilon$  to the Jacobian determinants as an

overcorrection. In our framework,  $\mathcal{L}_{Jdet}$  is a critical component since it ensures that the flow is diffeomorphic in  $\Omega$ . In this work, the Jacobian matrix is implemented as a discrete approximation of a smooth manifold.

The second term,  $\mathcal{L}_{mag}$ , regularizes the magnitude of the velocity field along the voxel cloud trajectory and is given by

$$\mathcal{L}_{mag} = \frac{1}{N} \int_0^s \|\mathcal{K} \mathbf{v}_\theta(q(t), t)\|_2^2 dt. \quad (9)$$

This amounts to penalising the *energy* of the flow. In practice, the integral is replaced by a summation of the squared norm along the steps taken by the numerical integration scheme. Lastly, the third term,  $\mathcal{L}_{smt}$ , is used regularize the spatial gradients of the transformed voxel cloud and is given by

$$\mathcal{L}_{smt} = \frac{1}{N} \sum_{\mathbf{x} \in q(s)} (\|\nabla_\psi(\mathbf{x})\|_2^2), \quad (10)$$

where  $\nabla_\psi(\mathbf{x})$  denotes the spatial gradient around  $\mathbf{x}$  under the transformation  $\psi$ . This encourages spatial smoothness of the transformed voxel cloud. Similar to  $\mathcal{L}_{Jdet}$ ,  $\mathcal{L}_{smt}$  is implemented as a discrete approximation. Note that, even though  $\mathbf{v}_\theta$  already includes Gaussian filtering, which in turn translates to the spatial smoothness of  $\psi$ , the inclusion of  $\mathcal{L}_{smt}$  can reduce the degradation in smoothness as a result of numerical integration.

The last term in Eqn.(5),  $\mathcal{B}(\psi)$ , specifies the boundary condition for the transformation  $\psi$ . While our MRI registration tasks do not specify any boundary condition ( $\mathcal{B}(\psi) = 0$ ), we will demonstrate its effect through simple experiments on 2D images.

### 3.2. Neural Ordinary Differential Equations

Taking inspiration from the resemblance between residual networks and dynamical systems, Chen et al. [9] first introduced neural ordinary differential equations (NODEs) to approximate infinite depth neural networks. It aims to



learn the function  $f$  parameterized by  $\theta$  by defining a loss function of the following form

$$\mathcal{L}(z(t_1)) = \mathcal{L}\left(z_0 + \int_{t_0}^{t_1} f_\theta(z(t), t) dt\right). \quad (11)$$

From a system perspective, NODEs are continuous-time models that represent vector fields as neural networks. It has since been adapted as a universal framework for modeling high-dimensional spatiotemporally chaotic systems utilizing convolutional layers [15], demonstrating its ability to capture highly complex behaviors in space and time. Hence, we find it a suitable candidate for our registration task.

Since NODEs often require the numerical solver to take many steps to realize the flows, they are memory-inefficient if all gradients along the integration steps needs to be stored using traditional backpropagation. Hence Many recent works [9, 26] on NODEs have therefore focused on reducing the memory requirements for gradient propagation. Notably, the adjoint sensitivity method (ASM) has enabled constant memory gradient propagation for optimizing NODEs, and we adopt ASM in our work as well. While we will briefly describe ASM here, two proofs for its gradient convergence can be found in [9, 15].

While the loss function  $\mathcal{L}$  can be any differentiable function, we will describe ASM by assuming  $\mathcal{L}$  to be the mean squared error (MSE) between the resulting flow  $z(t_1)$  and the label  $z_l$  which is given by (11). The only reason we express MSE in this form is that it's more convenient for proving ASM convergence [15]. We can therefore formulate the following optimization problem

$$\begin{aligned} \min_{\theta} \quad & \mathcal{L}(z(t_1)) = \int_{t_0}^{t_1} \delta(t_1 - t) \|z(t) - z_l\|_2^2 dt, \\ \text{s.t.} \quad & \frac{dz}{dt} = f_\theta(z(t), t), \\ & z(t_0) = z_0, \end{aligned} \quad (12)$$

where  $\delta(\cdot)$  is the Dirac delta function which ensures that only the gradients of the loss function with respect to  $z$  at  $t = t_1$  gets propagated back. To propagate the gradient from the loss function to the parameters  $\theta$ , first we numerically solve the differential equation  $dz/dt = f_\theta(z(t), t)$  for its trajectory forwards in time from  $t_0$  to  $t_1$  with the initial condition  $z(t_0) = z_0$ . Then we can define the adjoint equation given by:

$$\frac{d\lambda^T}{dt} = -\lambda^T \frac{\partial f}{\partial z} \Big|_{z=z(t)} + \frac{\partial \mathcal{L}}{\partial z} \Big|_{z=z(t)}, \quad (13)$$

where  $\lambda^T$  is a continuous-time Lagrange multiplier, also known as the adjoint variable. In the case of MSE, we have  $\partial \mathcal{L} / \partial z = 2 \cdot \delta(t_1 - t)(z(t) - z_l)$ . We then numerically solve this equation backwards in time with the initial condition

$\lambda^T(t_1) = 0$  to obtain the trajectory of  $\lambda^T$  from  $t = t_1$  to  $t = t_0$ . Lastly the gradient of the loss function with respect to the parameters, also known as the sensitivity is given by

$$\frac{d\mathcal{L}}{d\theta} = - \int_{t_0}^{t_1} \lambda^T \frac{\partial f}{\partial \theta} \Big|_{\theta=\theta(t)} dt. \quad (14)$$

After obtaining this gradient, we can then perform optimization with methods such as gradient descent. Note that the Jacobians  $\partial f / \partial x$  and  $\partial f / \partial \theta$  can be computed efficiently using automatic differentiation during the forward pass. In summary, ASM solves for gradients through the following steps:

- Numerically solve  $dz/dt = f_\theta(z, t)$  forward in time from  $t_0$  to  $t_1$ .
- Numerically solve the adjoint equation (13) backward in time from  $t_1$  to  $t_0$  using the initial condition  $\lambda^T(t_1) = 0$ .
- Numerically evaluate the integral in Eqn. (14) to obtain the desired gradient.

ASM enables our framework to interpolate between  $t = 0$  and  $t = s$  for an arbitrary number of steps with constant memory cost. This is particularly helpful when a temporally smooth diffeomorphic flow is required, as the numerical solver can increase its number of steps to improve the smoothness of  $q(t)$  with respect to  $t$ . Our implementation of ASM adapts from [23].

### 3.3. Illustrative Examples in 2D

To demonstrate the properties and capabilities of our framework, we used it to perform registration on a variety of 2D example images ( $\Omega \subseteq \mathbb{R}^2$ ) as shown in Figure 1 and Figure 3. The 2D brain images have size  $144 \times 160$ , and are slices taken from real 3D MRI. All other images have size  $144 \times 144$ , and were hand-drawn. Since these examples are fairly simple, we used MSE as the similarity loss and did not include  $\mathcal{L}_{mag}$  and  $\mathcal{L}_{smt}$ . Figure 3 shows the effect of Gaussian smoothing and  $\mathcal{L}_{Jdet}$  regularizer on 2D images. In addition, based on Figure 1, we note that the resulting transformation  $\psi$  is

**topology preserving:** While the framework warps the moving image as much as possible to look like the fixed image, it preserves the topology of the moving image in 2D. Columns (c) and (d) show that the warped ‘‘donut’’ closely resembles the circle, but the hole in its middle remains. Columns (g) and (h) illustrates the same concept as two disconnected components will not become connected.

**diffeomorphic in 2D:** Diffeomorphism is a stronger condition than the preservation of topology since it requires the transformation to be both continuous and differentiable. There are no visible holes or folds in the visualization of  $\psi$ . There are few violations if we inspect the Jacobian determinants of the resulting  $\phi$ , and this can be further reduced by increasing the weight on  $\mathcal{L}_{Jdet}$  at the expense of MSE. Note

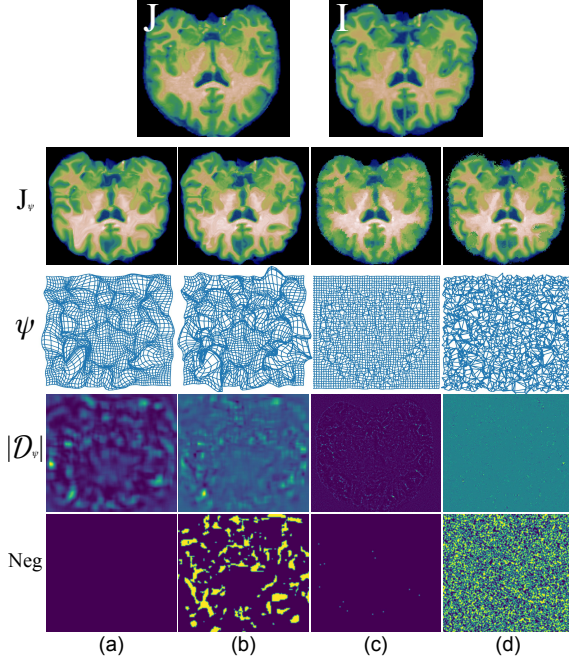


Figure 3: Demonstration of the effect of Gaussian smoothing  $\mathcal{K}$  and the  $\mathcal{L}_{Jdet}$  regularizer. The rows show ( $J_\psi$ ) warped moving images, ( $\psi$ ) grid visualization of the deformation field, ( $|D_\psi|$ ) Jacobian determinants of the transformation  $\psi$ , and (Neg) the regions with negative Jacobian determinants (yellow). The columns shows registration with (a) both  $\mathcal{K}$  and  $\mathcal{L}_{Jdet}$ , (b) only  $\mathcal{K}$ , (c) only  $\mathcal{L}_{Jdet}$ , and (d) with neither.

that there actually exists no diffeomorphism between  $I$  and  $J$  for the examples in columns (e)(f) because the sharp corners make  $I$ 's manifold non-smooth. Even so, our framework produces a slightly rounded "cross", as the result of a smooth approximation of  $\psi$ .

**enforcing boundary conditions:** Columns (a) (c) (e) (g) (i) show registration without boundary conditions, while the remaining columns fix the grids on all four sides. It can be observed that with this boundary condition, the four sides of the resulting  $\psi$  remain unchanged.

## 4. Experiments

### 4.1. Datasets and Pre-processing

We follow state-of-the-art [19] and employ atlas-based registration for evaluation. In this work, the atlases/templates are used as fixed images. We randomly select a small number of images as atlases and use the remainder as moving images to be registered to fixed images. We conduct experiments on two datasets: OASIS and CANDI.

**OASIS:** The OASIS [17] dataset consists of a collection of cross-sectional T1-weighted MRI scans from 416 subjects. These subjects are aged 18-96 where 100 of them have been clinically diagnosed with very mild to moderate Alzheimer's disease. We use standard processing tool FreeSurfer [13] to resample all MRI scans to  $1mm \times 1mm \times 1mm$ , followed by motion correction and skull stripping. We use the whole brain auto-segmentation provided in FreeSurfer for evaluation. Then we align all images and their segmentations to MNI 152 space [13] by affine transformation. The final images have a size of  $160 \times 192 \times 144$  by center cropping.

We set five images with IDs 1, 10, 20, 30, 40 as the atlases, and the remaining images with IDs  $< 50$ , as moving images. The total number of moving images is 40, resulting in 200 pairs to be registered.

**CANDI:** The Child and Adolescent NeuroDevelopment Initiative (CANDI) [16] dataset contains T1-weighted MRI scans of 4 groups, which are Healthy Controls, Schizophrenia Spectrum, Bipolar Disorder, and Bipolar Disorder without Psychosis. We use manually-labeled whole brain segmentation provided in the dataset for skull stripping. Then we transform images along with their respective segmentations to the MNI 152 space and center crop the images to the size  $160 \times 192 \times 144$  similar to the OASIS set.

We set the first subject of each group as the atlases (fixed images), and the following 5 subjects as moving images. The total number of moving images is 20, resulting in 80 pairs for registration.

### 4.2. Evaluation Metric

Deformable image registration (DIR) has no golden standard optimal solution since the two images to be registered usually do not share the same topology. The goal of DIR is to define the spatial correspondence such that the similarity of two images is maximized. In diffeomorphic registration, voxels are not allowed to fold or self-intersect, which can be guaranteed when the determinants of the Jacobian of the deformation field  $\mathcal{D}_\psi(x)$  are non-negative. We measure similarity and diffeomorphism using the following two criteria.

**Dice Similarity Coefficient :** The dice score measures the ratio between the overlap and union of two spatial regions. Here we calculate dice using the whole-brain segmentation maps. In particular, we evaluate dice between the fixed segmentation and the warped moving segmentation based on the deformation field given by the registration of the two images. For the OASIS dataset, we use auto-segmentation maps and compute the average dice across 28 anatomical structures as in VoxelMorph [6]. For the CANDI dataset, as it provides manual labels for 32 structures, we report the average dice for both 28 and 32 structures. One can refer to Figure. 4 for details of these anatomical structures.

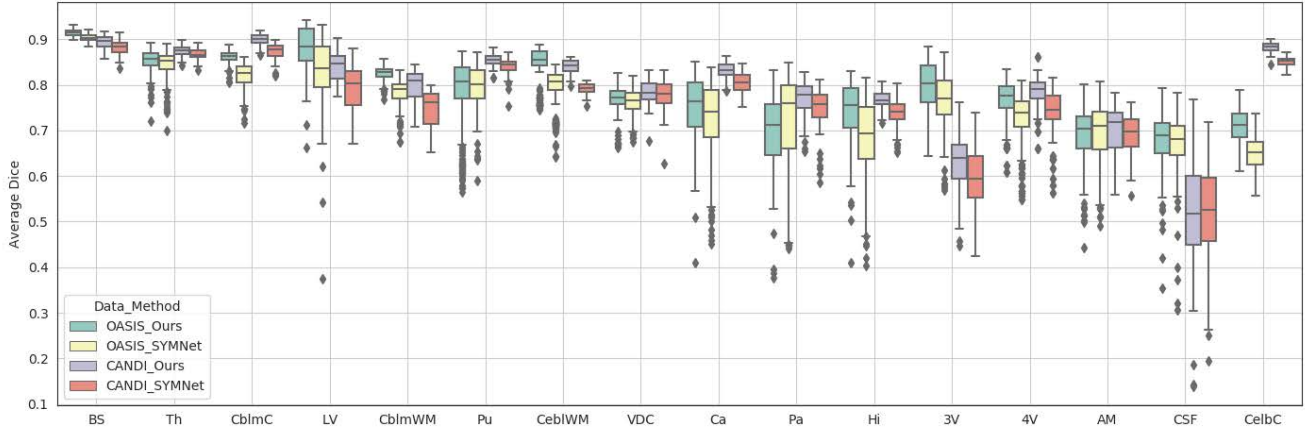


Figure 4: Boxplots indicating Dice for 28 anatomical structures on OASIS and CANDI datasets for SYMNet and our method. The abbreviations here represent brain stem (BS), thalamus (Th), cerebellum cortex (CblmC), lateral ventricle (LV), cerebellum white matter (CblmWM), putamen (Pu), cerebral white matter (CblWM), Ventral DC (VDC), caudate (Ca), pallidum (Pa), hippocampus (Hi), 3rd ventricle (3V), 4rd ventricle (4V), amygdala (AM), CSF (CSD), cerebral cortex (CelbC).

Table 1: **Comparison with state of the art.** The top part of this table shows results reported in the original SOTA paper [19]. The middle part shows results on our OASIS data setting, dice is averaged over 28 structures. The bottom part shows results on our CANDI data setting, we report both mean dice on 28 and 32 structures. Numbers here are represented as mean  $\pm$  std.

OASIS reported in [19]	Avg. Dice $\uparrow$	$\mathcal{D}_\psi(x) \leq 0 \downarrow$
Affine	$0.567 \pm 0.180$	-
DIF-VoxelMorph [10]	$0.693 \pm 0.156$	$0.008\% \pm 0.016$
VoxelMorph [6]	$0.727 \pm 0.144$	$2.626\% \pm 2.006$
SYMNet [19]	$0.743 \pm 0.113$	$0.026\% \pm 0.046$
OASIS dataset	Avg. Dice $\uparrow$	$\mathcal{D}_\psi(x) \leq 0 \downarrow$
SyN [5]	$0.729 \pm 0.109$	$0.026\%$
SYMNet [19]	$0.759 \pm 0.090$	$1.7 \times 10^{-4}\% \pm 2.0 \times 10^{-4}$
ours	<b><math>0.784 \pm 0.027</math></b>	$0.344\% \pm 0.145$
CANDI dataset	Avg. Dice $\uparrow$	$\mathcal{D}_\psi(x) \leq 0 \downarrow$
SyN (32 structures) [5]	$0.713 \pm 0.177$	$0.018\%$
SYMNet [19] (32 structures)	$0.736 \pm 0.015$	$1.4 \times 10^{-4}\% \pm 2.4 \times 10^{-4}$
ours (32 structures)	<b><math>0.763 \pm 0.151</math></b>	$0.080\% \pm 0.029$
SyN (28 structures) [5]	$0.739 \pm 0.102$	same as above
SYMNet [19] (28 structures)	$0.778 \pm 0.091$	same as above
ours (28 structures)	<b><math>0.804 \pm 0.092</math></b>	same as above

**Jacobian Determinant:** In our experiment, we report the negative Jacobian ratio denoted as  $r^{\mathcal{D}}$ , which represents the number of voxels with negative Jacobian determinants versus the total number of voxels for each image.

### 4.3. Comparison with state of the arts (SOTA)

We compare our proposed method with Symmetric Normalization (SyN) [5] and SYMNet [19]. SyN is a top-performing existing pair-wise optimization algorithm pro-

vided in the popular software package ANTs [1]. SYMNet is considered the leading learning based framework for image registration since it outperforms existing representative learning based methods such as the series of VoxelMorph works [6, 10]. Using a deep learning framework to learn the symmetric time 0.5 deformation fields, SYMNet achieves reversible registration and yields the best performance in terms of registration accuracy (dice) and quality of the deformation fields measured by  $r^{\mathcal{D}}$ . To enable a fair comparison with SYMNet, we employ the same dataset, *e.g.*, OASIS, and data processing practices and use the pre-trained model provided in the official SYMNet repository.

The quantitative results are shown in Table 1. Our method here uses 1 time steps, and 250 iterations for training. We report the original OASIS results [19] in the top part of Table 1. For both the OASIS and CANDI datasets, our method demonstrates a consistent and significant improvement in both mean dice scores over the all brain structures as shown in Table 1, and on each anatomical category as shown in Figure 4. Our  $r^{\mathcal{D}}$  (all  $\leq 0.1\%$ ) verifies that our method effectively preserves the topology. We visualize the qualitative result of the registration for one example pair image (OASIS-001 and OASIS-002) in Figure 5. We can observe that the ventricle area of the warped brain image obtained with our method is much clearer and does not show any phantom artifacts (cloudy regions where it is black in the fixed image). Note that we evaluated the performance of the pre-trained SYMNet by directly doing inference on its training data, giving it some unfair advantage in terms of inference performance. Nevertheless, our method still outperforms both SOTA pair-wise optimization (SyN) and

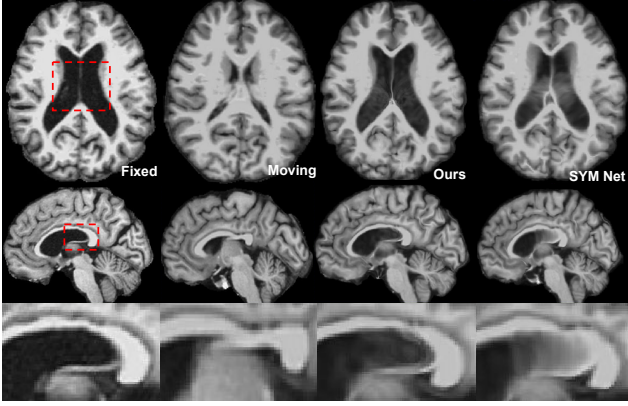


Figure 5: Images showing an example of a registration image pair. Fixed image is OASIS ID001 and Moving image is OASIS ID002. The 3rd column is ours warped image after registration and the 4th column is result of SYMNet [19].

learning based (SYMNet) methods.

It is important to note that the OASIS dataset generally presents larger deformations between images compared with the CANDI dataset because of the larger age range of the subjects. Therefore we can see lower dice scores for the 28 structures in the OASIS set compared to the CANDI set and more violations of diffeomorphism. Also, note that 4 out of the 32 structures on CANDI are very small, which are inherently difficult for alignment in registration due to their lower spatial smoothness. This explains the lower dice on the 32 structures compared with that of the 28 structures.

Lastly, we compare the running time of our method with the SOTA methods. While the SYMNet takes about 2 seconds to complete registration for one image pair, the pairwise optimization based method SyN takes 20 to 30 minutes to complete. In comparison, our method only takes approximately 97 seconds for one pair of registration (1 step taken), which is a significant improvement compared with SOTA optimization based approaches.

## 4.4. Method Analysis

### 4.4.1 Effect of time steps and training iteration

While our demos on 2D images use non-autonomous ODEs, we use autonomous ODEs for registering 3D MRI images and leave the non-autonomous version for future work. Table 2 shows that increasing the number of time steps does not impact the registration performance. This is a direct consequence of having a stationary velocity field in the Eulerian frame. We hypothesize that this should not be the case for a non-stationary velocity field because increasing the number of time steps will improve the model expressiveness by giving it more “temporal memory”.

Table 2: **Results of different time steps and optimization iterations.** Numbers here show dice score, negative Jacobian ratio, runtime (seconds) respectively.

time steps	200 iters	250 iters	300 iters
1-steps	0.797 / 0.37% / 79	0.802 / 0.39% / 97	0.803 / 0.37% / 120
2-steps	0.795 / 0.38% / 123	0.801 / 0.38% / 148	0.803 / 0.37% / 180
3-steps	0.800 / 0.39% / 166	0.802 / 0.38% / 199	0.802 / 0.39% / 248
4-steps	0.800 / 0.40% / 210	0.802 / 0.39% / 260	0.801 / 0.37% / 311
5-steps	0.801 / 0.38% / 249	0.800 / 0.39% / 318	0.802 / 0.37% / 375

Table 3: **Results of different representations of velocity field.**  $N$  represents the total number of voxels. Note ours learning number of parameters are constant regarding the number of time steps. We show results for tensor velocity field with and without Gaussian Kernel  $\mathcal{K}$ .

Rep of Velocity Field	Avg. DSC	$\mathcal{D}_\psi(\mathbf{x}) \leq 0$	# parameters
ours network 1 step	0.803	0.37%	0.83 $N$
Tensor w $\mathcal{K}$ 1 step	0.769	0.90%	$N$
Tensor w $\mathcal{K}$ 2 step	0.757	0.90%	2 $N$
Tensor w $\mathcal{K}$ 3 step	0.755	0.90%	3 $N$
Tensor w/o $\mathcal{K}$ 1 step	0.553	5.24%	$N$
Tensor w/o $\mathcal{K}$ 2 step	0.553	5.26%	2 $N$
Tensor w/o $\mathcal{K}$ 3 step	0.554	5.28%	3 $N$

### 4.4.2 Representation of velocity field

Given our framework’s flexibility in model choice, we experimented with different representations of  $\mathbf{v}_\theta$  with the results given in Table 3. In particular, besides the architecture shown in Figure 2, we also optimize a tensor directly to model the velocity field at every time step taken. Note that in this case the velocity is time-varying as we search for a different tensor at every step, as indicated in Table 3, where the number of parameters increase linearly with the number of steps taken. This tensor representation of velocity fields is consistent with LDDMM but with the difference that LDDMM uses different optimization approaches. Our results show that the neural network proposed in Figure 2 works the best in terms of both the average dice score and  $r^{\mathcal{D}}$ .

## 5. Conclusion

We have presented a fast and generic optimization based method for deformable image registration. This effort is still in its early stages and many aspects remain to be explored. But our experiments demonstrate its promising aspects in terms of both registration accuracy and speed. For future work, we hope to extend this work to multi-resolution image registration to further improve its speed. In addition, we will consolidate non-autonomous ODE representation of velocity fields on 3D images by exploring different ways of time injection to the neural network. Other possible directions include exploring the framework’s potential link to and integration with different optimization techniques.



## References

- [1] <https://github.com/ANTsX/ANTsPy>.
- [2] Daniel H Adler, Laura EM Wisse, Ranjit Ittyerah, John B Pluta, Song-Lin Ding, Long Xie, Jiancong Wang, Salmon Kadivar, John L Robinson, Theresa Schuck, et al. Characterizing the human hippocampus in aging and alzheimer's disease using a computational atlas derived from ex vivo mri and histology. *Proceedings of the National Academy of Sciences*, 115(16):4252–4257, 2018.
- [3] Moab Arar, Yiftach Ginger, Dov Danon, Amit H Bermano, and Daniel Cohen-Or. Unsupervised multi-modal image registration via geometry preserving image-to-image translation. In *Proceedings of the IEEE/CVF conference on computer vision and pattern recognition*, pages 13410–13419, 2020.
- [4] Vincent Arsigny, Olivier Commowick, Xavier Pennec, and Nicholas Ayache. A log-euclidean framework for statistics on diffeomorphisms. In Rasmus Larsen, Mads Nielsen, and Jon Sporring, editors, *Medical Image Computing and Computer-Assisted Intervention - MICCAI 2006, 9th International Conference, Copenhagen, Denmark, October 1-6, 2006, Proceedings, Part I*, volume 4190 of *Lecture Notes in Computer Science*, pages 924–931. Springer, 2006.
- [5] Brian B Avants, Charles L Epstein, Murray Grossman, and James C Gee. Symmetric diffeomorphic image registration with cross-correlation: evaluating automated labeling of elderly and neurodegenerative brain. *Medical image analysis*, 12(1):26–41, 2008.
- [6] G. Balakrishnan, A. Zhao, M. R. Sabuncu, A. V. Dalca, and J. Guttag. An unsupervised learning model for deformable medical image registration. In *CVPR*, pages 9252–9260, 2018.
- [7] M Faisal Beg, Michael I Miller, Alain Trouvé, and Laurent Younes. Computing large deformation metric mappings via geodesic flows of diffeomorphisms. *International journal of computer vision*, 61(2):139–157, 2005.
- [8] Y. Cao, Shengtai Li, L. Petzold, and R. Serban. Adjoint sensitivity analysis for differential-algebraic equations: The adjoint dae system and its numerical solution. *SIAM J. Sci. Comput.*, 24:1076–1089, 2003.
- [9] Tian Qi Chen, Yulia Rubanova, Jesse Bettencourt, and David Duvenaud. Neural ordinary differential equations. In Samy Bengio, Hanna M. Wallach, Hugo Larochelle, Kristen Grauman, Nicolò Cesa-Bianchi, and Roman Garnett, editors, *NeurIPS*, pages 6572–6583, 2018.
- [10] Adrian V Dalca, Guha Balakrishnan, John Guttag, and Mert R Sabuncu. Unsupervised learning for fast probabilistic diffeomorphic registration. In *International Conference on Medical Image Computing and Computer-Assisted Intervention*, pages 729–738. Springer, 2018.
- [11] Adrian V Dalca, Guha Balakrishnan, John Guttag, and Mert R Sabuncu. Unsupervised learning of probabilistic diffeomorphic registration for images and surfaces. *Medical image analysis*, 57:226–236, 2019.
- [12] Adrian V Dalca, Marianne Rakic, John Guttag, and Mert R Sabuncu. Learning conditional deformable templates with convolutional networks. *IEEE TMI: Transactions on Medical Imaging*, 2019.
- [13] Bruce Fischl. Freesurfer. *Neuroimage*, 62(2):774–781, 2012.
- [14] James C Gee, Martin Reivich, and Ruzena Bajcsy. Elastically deforming a three-dimensional atlas to match anatomical brain images. 1993.
- [15] Tom Z. Jiahao, M. Ani Hsieh, and Eric Forgoston. Learning nonlinear dynamics and chaos: A universal framework for knowledge-based system identification and prediction, 2020.
- [16] David N Kennedy, Christian Haselgrove, Steven M Hodge, Pallavi S Rane, Nikos Makris, and Jean A Frazier. Candishare: a resource for pediatric neuroimaging data, 2012.
- [17] Daniel S Marcus, Tracy H Wang, Jamie Parker, John G Csernansky, John C Morris, and Randy L Buckner. Open access series of imaging studies (oasis): cross-sectional mri data in young, middle aged, nondemented, and demented older adults. *Journal of cognitive neuroscience*, 19(9):1498–1507, 2007.
- [18] Michael I Miller, Alain Trouvé, and Laurent Younes. Geodesic shooting for computational anatomy. *Journal of mathematical imaging and vision*, 24(2):209–228, 2006.
- [19] Tony CW Mok and Albert Chung. Fast symmetric diffeomorphic image registration with convolutional neural networks. In *CVPR*, pages 4644–4653, 2020.
- [20] Zhengyang Shen, Xu Han, Zhenlin Xu, and Marc Niethammer. Networks for joint affine and non-parametric image registration. In *Proceedings of the IEEE/CVF Conference on Computer Vision and Pattern Recognition*, pages 4224–4233, 2019.
- [21] A. Sotiras, C. Davatzikos, and N. Paragios. Deformable medical image registration: A survey. *IEEE Transactions on Medical Imaging*, 32(7):1153–1190, 2013.
- [22] Steven H. Strogatz. *Nonlinear Dynamics and Chaos: With Applications to Physics, Biology, Chemistry and Engineering*. Westview Press, 2000.
- [23] Mikhail Surtsukov. neural-ode. <https://github.com/msurtsukov/neural-ode>, 2019.
- [24] Quanxin Wang, Song-Lin Ding, Yang Li, Josh Royall, David Feng, Phil Lesnar, Nile Graddis, Maitham Naeemi, Benjamin Facer, Anh Ho, et al. The allen mouse brain common coordinate framework: a 3d reference atlas. *Cell*, 181(4):936–953, 2020.
- [25] Xiao Yang, Roland Kwitt, Martin Styner, and Marc Niethammer. Quicksilver: Fast predictive image registration—a deep learning approach. *NeuroImage*, 158:378–396, 2017.
- [26] Juntang Zhuang, Nicha Dvornek, Xiaoxiao Li, Sekhar Tatikonda, Xenophon Papademetris, and James Duncan. Adaptive checkpoint adjoint method for gradient estimation in neural ode. In *International Conference on Machine Learning*, pages 11639–11649. PMLR, 2020.